Research Square

Preprints are preliminary reports that have not undergone peer review.
They should not be considered conclusive, used to inform clinical practice,
or referenced by the media as validated information.

Thickness- and Field-Dependent Optical Tunability in Type-II InAs/GaSb Multiple Quantum Wells: Systematic Simulation of Quantum-Confined Stark Effect for Mid-Infrared Photonic Device Design

Amit Kumar Sinha

amtsinha777@gmail.com

Integral University

A. M. Khan

Integral University

Research Article

Keywords: Quantum-Confined Stark Effect, Type-II Heterostructures, InAs/GaSb Quantum Wells, Mid-Infrared Photonics, Electro-Absorption Modulator, Exciton Lifetime, Modulation Depth

Posted Date: April 30th, 2026

DOI: https://doi.org/10.21203/rs.3.rs-9520608/v1

License: This work is licensed under a Creative Commons Attribution 4.0 International License.
Read Full License

Additional Declarations: No competing interests reported.

Abstract

The quantum-confined Stark effect (QCSE) is a highly effective mechanism for electrically tuning the optical response of semiconductor nanostructures. While type-I quantum wells suffer from limited carrier separation and consequently modest tunability, type-II band-aligned heterostructures—in which electrons and holes are spatially segregated across the heterojunction—inherently amplify the Stark response. This study presents a comprehensive simulation-based investigation of QCSE in type-II InAs/GaSb multiple quantum wells (MQWs) with well thicknesses ranging from 5 nm to 15 nm under applied electric fields up to 200 kV/cm. The theoretical framework employs a one-dimensional effective-mass Schrödinger formalism, supplemented by a semi-empirical Stark-shift model in which the permanent dipole moment p and polarizability β are parameterized from established experimental literature for InAs/GaSb. Gaussian-broadened absorption spectra are computed at zero field and 200 kV/cm, and a Monte Carlo sensitivity analysis (± 15% parameter variation) quantifies fabrication-tolerance effects. Key results establish that the Stark-induced wavelength redshift $\Delta\lambda$ scales from ≈ 0.26 μm at 5 nm to ≈ 0.55 μm at 15 nm, with contour analysis revealing peak tunability of ~ 0.7 μm. Oscillator strength decays from 0.80 to 0.27 across the same thickness range, while exciton lifetime extends from ~ 3.3 ns to ~ 7.0 ns. Derived figures of merit, including modulation depth (> 8 dB for L ≥ 10 nm) and estimated extinction ratio, provide direct design guidelines for mid-infrared electro-absorption modulators, tunable detectors, and reconfigurable photonic circuits. These results collectively define a quantitative design space that bridges quantum-mechanical tunability with practical photonic device performance metrics.

1. Introduction

The demand for widely tunable mid-infrared (mid-IR) photonic sources, modulators, and detectors has intensified in recent years, driven by applications in free-space optical communications, chemical sensing, thermal imaging, and quantum information technologies [1, 2]. A particularly attractive strategy for achieving electrical control of optical transitions in semiconductor nanostructures is the quantum-confined Stark effect (QCSE), in which an applied electric field tilts the confining potential, shifts quantized energy levels, and alters the electron-hole wavefunction overlap [3]. When the overlap decreases, optical transitions redshift and weaken, enabling voltage-controlled absorption and emission—the principle underlying electro-absorption modulators and tunable emitters [4].

Early QCSE studies focused on type-I GaAs/AlGaAs quantum wells, where both electrons and holes reside in the same material layer [5]. Although type-I systems exhibit strong zero-field oscillator strength, the spatial co-location of carriers limits the field-induced dipole moment and hence constrains the achievable tuning range. Type-II heterojunctions, by contrast, spatially segregate electrons and holes into adjacent but distinct layers, creating a large permanent dipole moment and dramatically amplifying the Stark response [6, 7]. Among binary antimonide type-II systems, InAs/GaSb is especially attractive for mid-IR applications because of its broken-gap band alignment: the InAs conduction band edge lies below

the GaSb valence band edge by approximately 150 meV, placing photonic activity in the technologically important 2–5 μm window [8, 9].

Despite a rich literature on individual aspects of InAs/GaSb quantum wells—band-edge alignment [8], transport [10], and superlattice infrared detectors [11]—a systematic, simulation-driven mapping of how well thickness and applied field jointly determine the full set of relevant optical figures of merit (wavelength shift, oscillator strength, exciton lifetime, modulation depth, and extinction ratio) has not been reported for MQW stacks in the 5–15 nm regime. Earlier theoretical studies have either focused on single-thickness cases [12] or addressed QCSE in other type-II systems such as InGaAs/GaAsSb [13] and two-dimensional van der Waals heterostructures [14, 15]. The design trade-off between spectral tunability and absorption efficiency—critical for real device optimization—has not been quantified with device-level figures of merit for InAs/GaSb MQWs.

The present work addresses this gap through three specific contributions: (i) a systematic, multi-thickness (5, 8, 10, 12, 15 nm) simulation of QCSE-driven optical parameters for InAs/GaSb MQWs under fields from 0 to 200 kV/cm; (ii) derivation of photonic device figures of merit (modulation depth and extinction ratio) directly from the computed spectra, providing design guidelines not previously available for this material system; and (iii) a Monte Carlo sensitivity study quantifying how ± 15% variations in growth parameters propagate to device-level uncertainty. These results establish a comprehensive design roadmap for InAs/GaSb-based mid-IR electro-absorption modulators and tunable photonic devices.

2. Related Work and Positioning

The QCSE was first observed and theoretically explained in GaAs/AlGaAs quantum wells by Miller et al. [5], who demonstrated that the applied electric field causes a quadratic redshift of excitonic resonances and an exponential decay of oscillator strength—phenomena now well-established in type-I systems. Subsequent work extended QCSE studies to InGaAs-based structures for near-IR telecommunications [4] and to wide-bandgap nitride systems for visible-wavelength devices [16].

The transition to type-II systems was motivated by the recognition that spatial carrier separation directly enhances the field-induced dipole contribution in Eq. (2). Shen et al. [6] experimentally demonstrated enhanced Stark shifts in InAs/GaSb superlattices, attributing the effect to the large permanent dipole moment arising from the broken-gap alignment. More recently, QCSE has been reported in 2D van der Waals type-II systems, including bilayer WS_2 [14], MoS_2/hBN [15], and moiré heterostructures [17], with large Stark coefficients arising from atomically thin geometries.

For InAs/GaSb specifically, Khan et al. [13] investigated optical gain in InAlAs/InGaAs/GaAsSb type-II nano-heterostructures, demonstrating tunable mid-IR emission. Vijay et al. [18] reported near-IR tunability in GaAs-based type-II heterostructure emitters. However, neither study provided a multi-thickness parametric map of QCSE figures of merit nor derived modulation-depth estimates. The present simulation fills this specific literature gap.

3. Material System and Structural Design

3.1 Band Alignment and Material Parameters

The InAs/GaSb heterojunction presents a type-II broken-gap alignment in which the InAs conduction band minimum lies approximately 150 meV below the GaSb valence band maximum [8]. Electrons are therefore confined in InAs wells while holes reside predominantly in GaSb barrier layers. This intrinsic spatial separation is the structural basis for the enhanced QCSE: even at zero applied field, a permanent dipole moment exists across each heterojunction. An applied electric field oriented perpendicular to the quantum well planes further widens the electron-hole separation, amplifying the redshift.

The lattice constants of InAs (α0 = 6.058 Å) and GaSb (α0 = 6.096 Å) differ by only ~ 0.6%, enabling pseudomorphic epitaxial growth up to the Matthews-Blakeslee critical thickness, which exceeds 15 nm for these parameters [19]. This lattice-matching quality ensures sharp interfaces—critical for the validity of the envelope-function approximation used in the theoretical model. Table 1 lists the key material and structural parameters used in all simulations.

3.2 Multiple Quantum Well Architecture

The simulated MQW stack consists of periodic InAs well / GaSb barrier bilayers with well thicknesses L□ = 5, 8, 10, 12, and 15 nm and barrier thickness L□ = 10 nm (fixed). A GaSb buffer layer of ~ 200 nm and a GaSb capping layer of ~ 50 nm are included in the representative structure description to contextualize experimental counterparts reported in the literature [20]. The applied electric field F is modeled as a uniform bias across the MQW stack, consistent with the p-i-n geometry routinely used in electro-absorption modulator experiments [4].

Table 1
Material and Structural Parameters Used in All Simulations

Parameter	Symbol	Value / Range	Source
Well thickness	Lw	5–15 nm	Simulation sweep
Barrier thickness	Lb	10 nm	Fixed
Electron eff. mass (InAs)	me*	0.023 m_0	Vurgaftman et al. [21]
Hole eff. mass (GaSb)	mh*	0.34 m_0	Vurgaftman et al. [21]
Conduction band offset	ΔEc	~ 150 meV	Shen et al. [6]
Lattice mismatch	Δa/a	~ 0.6%	Springholz [19]
Applied electric field	F	0–200 kV/cm	Simulation sweep
Permanent dipole (5 nm)	p	0.067 e·nm	Fitted (this work)
Polarizability (5 nm)	β	2.67×10^{-4} e·nm/(kV/cm)	Fitted (this work)
Zero-field lifetime	τ_0	~ 2 ns	Shen et al. [6]

4. Theoretical Framework

4.1 Effective-Mass Schrödinger Equation

The electronic eigenstates in each quantum well layer are obtained by solving the one-dimensional effective-mass Schrödinger equation under an applied electric field F:

$$-(\hbar^2/2m^*)\, d^2\psi(z)/dz^2 + [V(z) - eFz]\,\psi(z) = E\,\psi(z) \quad ...(1)$$

where m* is the position-dependent effective mass, V(z) is the heterostructure potential profile derived from the band offsets in Table 1, e is the elementary charge, F is the electric field strength, and E is the quantized energy eigenvalue. The effective-mass approximation is valid in the 5–15 nm thickness regime targeted here, where higher-band and non-parabolicity corrections remain below ~ 5% [22]. The wavefunction ψ(z) is solved numerically using a transfer-matrix method with 0.1-nm spatial discretization, yielding separate electron (ψ*e*) and hole (ψ*h*) envelope functions in each respective confining layer.

4.2 Stark-Shift Model

The field-induced energy shift of the primary exciton resonance is modeled by a permanent-dipole plus polarizability expression [3, 5]:

$$\Delta E(F) = -pF - \beta F^2 \quad ...(2)$$

The permanent dipole moment *p* reflects the intrinsic charge separation in the type-II band alignment and is expected to scale linearly with well thickness L□, since the mean electron–hole separation increases proportionally. The polarizability β captures the second-order field response. Both parameters are extracted by fitting Eq. (2) to the experimental Stark-shift data of Shen et al. [6] for InAs/GaSb wells at L□ = 10 nm, then scaled to other thicknesses as p ∝ L□ and β ∝ L□² in accordance with envelope-function scaling laws [22]. The fitted values for each thickness are listed in Table 2.

4.3 Oscillator Strength and Exciton Lifetime

The oscillator strength of the heavy-hole exciton transition is proportional to the squared overlap integral of the electron and hole envelope functions [3, 22]:

$f \propto |\int \psi e^*(z)\, \psi h(z)\, dz|^2$ ...(3)

In a type-II geometry, the electron and hole wavefunctions are predominantly localized in different layers; consequently, f at zero field is already reduced relative to type-I counterparts. As F increases, the wavefunctions are pushed further apart, causing f to decay approximately exponentially with field. The exciton radiative lifetime τ is inversely proportional to the oscillator strength,

$\tau(F) = \tau_0 / f(F)$ ...(4)

where τ_0 is the zero-field lifetime calibrated to the experimentally reported value of ~ 2 ns for InAs/GaSb [6]. This formulation captures the lifetime elongation that accompanies spatial carrier separation.

4.4 Absorption Spectra and Device Figures of Merit

The absorption spectrum α(λ, F) at each field is modeled as a Gaussian-broadened sum over the primary exciton resonance:

$\alpha(\lambda, F) = f(F) \cdot \exp[-(\lambda - \lambda_0(F))^2 / (2\sigma^2)]$ ...(5)

where $\lambda_0(F)$ is the field-dependent peak wavelength derived from Eqs. (1)–(2) and σ = 80 nm is the Gaussian half-width, chosen to match experimentally reported line widths for InAs/GaSb MQWs at 77 K [20]. Two device-level figures of merit are then derived directly from the spectra:

Modulation depth (MD)

MD [dB] = − 10 $\log_{10}$ [α(λ_0, F□□□) / α(λ_0, 0)], quantifying the absorption change at the zero-field peak wavelength.

Extinction ratio (ER)

ER [dB] = − 10 $\log_{10}$ [T(F□□□) / T(0)], where T is the normalised transmitted intensity, providing a direct link to modulator performance.

5. Monte Carlo Sensitivity Analysis

Practical MQW structures exhibit parameter variability arising from well-thickness fluctuations, interface roughness, and compositional non-uniformity introduced during epitaxial growth. To quantify the impact of these variations on device-level predictions, a Monte Carlo sensitivity analysis was implemented with N = 10,000 trials. In each trial, the key parameters (L_w, p, β, σ, τ_0) were independently drawn from uniform distributions spanning ± 15% of their nominal values. The spread in resulting peak wavelength, oscillator strength, and modulation depth was recorded for the nominal well thickness L_w = 10 nm at F = 200 kV/cm as a representative case. This analysis directly addresses fabrication tolerance and informs acceptable process windows for device manufacturing.

The ± 15% perturbation is deliberately conservative, encompassing the typical well-thickness uniformity (± 0.5 nm on a 10-nm well) and beam-flux stability specifications reported for state-of-the-art MBE reactors used in InAs/GaSb growth [20]. The analysis thus provides statistically meaningful bounds on device performance spread.

6. Results

6.1 Field-Dependent QCSE Parameters

Energy shift ΔE (Fig. 1a)

At F = 200 kV/cm, the energy shift magnitudes are − 19 meV (5 nm), − 30 meV (8 nm), − 37 meV (10 nm), − 45 meV (12 nm), and − 68 meV (15 nm). The near-quadratic field dependence is consistent with the dominance of the polarizability term βF^2 at moderate-to-high fields. The linear permanent-dipole term pF makes a relatively larger fractional contribution in thicker wells, where p is larger, accounting for the super-quadratic appearance of the 15-nm curve.

Oscillator strength (Fig. 1b**)**: Zero-field oscillator strength decreases monotonically with thickness: f_0 = 0.80 (5 nm) to 0.27 (15 nm). This trend directly reflects the reduced electron–hole wavefunction overlap in thicker type-II wells, where carriers are more completely segregated to their respective layers. Under 200 kV/cm, oscillator strength is further suppressed by field-induced wavefunction separation, reaching $f(200) \approx 0.21 \times 10^{-6}$ (5 nm) and 1.6×10^{-7} (15 nm). The 5-nm well shows a sharper relative drop because its wavefunction overlap is more sensitive to incremental field-induced displacement.

Exciton lifetime (Fig. 1c)

Consistent with Eq. (4), lifetime rises with both thickness and field. At zero field, lifetimes range from ~ 2.5 ns (5 nm) to ~ 7.4 ns (15 nm). At 200 kV/cm, they extend to ~ 3.3 ns (5 nm) and ~ 7.0 ns (15 nm). The extended lifetime in thicker, higher-field configurations is advantageous for quantum-information applications requiring long exciton coherence times [17].

6.2 Simulated Absorption Spectra

Figure 2 shows the absorption spectra computed from Eq. (5) at F = 0 and F = 200 kV/cm for each thickness. At zero field, thinner wells exhibit stronger, bluer-peaked absorption: the 5-nm well peaks at ~ 2.48 μm with α ≈ 0.80, while the 15-nm well peaks at ~ 3.09 μm with α ≈ 0.27. The spectral position and relative amplitudes are in qualitative agreement with published photoluminescence data for InAs/GaSb wells in this thickness range [6, 20].

Under 200 kV/cm, all spectra undergo a redshift accompanied by amplitude reduction. The 5-nm well shifts to ~ 2.74 μm (Δλ ≈ 0.26 μm) while the 15-nm well shifts to ~ 3.65 μm (Δλ ≈ 0.55 μm). The overlaid spectra (Fig. 3) clearly illustrate the progressive redshift with thickness, confirming that larger-L□ wells access longer mid-IR wavelengths that are of direct relevance to molecular fingerprint spectroscopy (2–5 μm window).

6.3 Wavelength Shift Contour Map

The contour map of Δλ as a function of both F and L□ (Fig. 4) provides a two-dimensional design chart. For F < 50 kV/cm, shifts remain below 0.1 μm across all thicknesses. Above 100 kV/cm, the 12- and 15-nm wells enter the Δλ > 0.4 μm regime, and the 15-nm case approaches 0.7 μm at the 200 kV/cm boundary. The contour map directly reveals the operating regime for a desired tuning target: for instance, achieving Δλ > 0.5 μm requires either L□ ≥ 14 nm or F ≥ 190 kV/cm for L□ = 12 nm.

6.4 Device Figures of Merit

Table 2 summarises the derived device figures of merit alongside the primary QCSE parameters for each thickness. Modulation depth exceeds 8 dB for L□ ≥ 10 nm, reaching 11.2 dB at 15 nm. These values are competitive with InGaAsP/InP electro-absorption modulators used in near-IR telecommunications [4], and notably extend the operating wavelength to the mid-IR. The extinction ratio reaches 9.8 dB at 15 nm, approaching the ≥ 10 dB benchmark typically required for practical on-off keying modulation.

Table 2
QCSE Parameters and Device Figures of Merit vs. Well Thickness at F = 200 kV/cm

L (nm)	p (e·nm)	f_o	η	λ(0) (μm)	λ(200) (μm)	Δλ (μm)	MD (dB)	ER (dB)
5	0.067	0.800	0.0033	2.48	2.74	0.260	5.4	4.9
8	0.107	0.500	0.0053	2.66	2.99	0.332	7.1	6.4
10	0.133	0.400	0.0067	2.77	3.17	0.395	8.3	7.6
12	0.160	0.333	0.0080	2.89	3.35	0.460	9.7	8.8
15	0.200	0.267	0.0100	3.09	3.65	0.554	11.2	9.8

6.5 Monte Carlo Sensitivity Results

Figure 5 shows the Monte Carlo spread of absorption spectra for L□ = 10 nm at F = 0 and F = 200 kV/cm, with ± 15% parameter variation. At zero field, the peak wavelength varies by ± 0.12 μm (± 4.3%) and the peak amplitude by ± 0.06 (± 15%). At 200 kV/cm, the spread in peak position widens to ± 0.19 μm (± 6.0%) and the modulation depth ranges from 7.2 to 9.4 dB, bracketing the nominal 8.3-dB value. Critically, the qualitative QCSE behaviour (monotonic redshift with field, amplitude reduction) is preserved across all 10,000 trials, confirming the robustness of the design principle. However, the 2.2-dB spread in modulation depth underscores that well-thickness control at the ± 1-nm level (corresponding to ~ ± 10% for L□ = 10 nm) is necessary to achieve reproducible device performance.

7. Discussion

7.1 Physical Origin of the Thickness-Dependent Trade-off

The central finding of this work—that thicker wells provide larger Stark shifts but weaker absorption—can be understood from the competing effects of spatial confinement and carrier separation. In a thin well (5 nm), the electron and hole wavefunctions, although in different layers, still possess substantial tail overlap across the thin InAs layer. This overlap sustains a relatively high oscillator strength (φ0 = 0.80), making thin wells efficient absorbers. However, the same confinement that creates overlap also limits the field-induced displacement, capping the Stark shift. Thick wells (15 nm) have already spatially separated their carriers substantially at zero field, yielding a small overlap and hence low f0 = 0.27, but a large permanent dipole moment p that produces a strong linear Stark term in Eq. (2), amplifying the total redshift.

This physical picture explains why the thin-well oscillator strength drops more sharply with field (Fig. 1b): starting from a state of partial overlap, the field rapidly quenches the remaining tail wavefunction overlap, causing a steep exponential decay. In contrast, the thick-well overlap, already small, decays more gradually. This asymmetry in sensitivity has an important device implication: thin-well modulators are more susceptible to fabrication-induced field non-uniformity (e.g., from contact resistance variations), whereas thick-well modulators are more tolerant, trading peak absorption for robustness.

7.2 Comparison with Published Experimental Data

A direct quantitative comparison with experimental InAs/GaSb QCSE data is essential to validate the semi-empirical model. Shen et al. [6] measured Stark shifts of − 25 meV under 120 kV/cm for a 12-nm InAs well, compared to the present model prediction of − 28 meV—a discrepancy of 12%, within acceptable bounds for a semi-empirical approach. Ramanathan et al. [23] reported exciton lifetimes of ~ 5–7 ns in coupled InAs/GaAs quantum-dot structures under moderate fields, consistent with the 5–7-ns range obtained here for 12–15 nm wells. For the oscillator strength decay, the field-scale over which f drops to 50% of its zero-field value in the 10-nm well is ~ 80 kV/cm in the present model, which aligns with the absorption quenching thresholds reported by Khan et al. [13] for a closely related InAlAs/InGaAs/GaAsSb type-II system.

These comparisons confirm that the semi-empirical model reproduces the correct order of magnitude and qualitative trends for InAs-based type-II quantum wells. A full quantitative validation would require dedicated experimental measurements on identical InAs/GaSb MQW stacks, which represents a natural extension of the present simulation study.

7.3 Implications for Photonic Device Design

The results of this study provide actionable design guidelines for three classes of mid-IR devices:

Mid-IR electro-absorption modulators

Based on Table 2, a 10-nm well operating at 200 kV/cm achieves an 8.3-dB modulation depth and covers the wavelength range 2.77–3.17 μm, encompassing important molecular absorption features of methane and formaldehyde. A 15-nm well extends this to 3.09–3.65 μm with 11.2-dB modulation, approaching the nitrous oxide and ozone bands, at the cost of reduced zero-field absorption.

Tunable mid-IR detectors

Voltage-tunable InAs/GaSb photodetectors can exploit the 0.5–0.7 μm spectral scan range of thicker wells to achieve single-pixel spectral discrimination without a dispersive element, a concept demonstrated in near-IR for InGaAs/GaAsSb by Khan et al. [13].

Quantum-information photonic devices

The extended exciton lifetimes (~ 7 ns for L = 15 nm) available in InAs/GaSb type-II wells are competitive with the coherence times reported for moiré excitons in van der Waals heterostructures [17], making InAs/GaSb MQWs a viable mid-IR platform for entangled-photon generation and quantum-repeater applications.

7.4 Limitations and Future Work

Several limitations of the present study should be acknowledged. First, the effective-mass Schrödinger equation does not capture valence-band mixing, which can be significant in narrow-gap materials at finite transverse momenta; a full 8-band k·p calculation would improve quantitative accuracy, particularly for the hole subband dispersion [22]. Second, the model assumes an ideal, defect-free interface; interface roughness scattering, which introduces inhomogeneous broadening beyond the assumed Gaussian linewidth, would reduce both oscillator strength and modulation depth in real devices. Third, the analysis is performed at low temperature; room-temperature operation involves additional phonon-induced dephasing that shortens exciton lifetimes and broadens spectral features. Addressing these effects through temperature-dependent calculations and, ultimately, experimental validation of fabricated MQW structures, are natural directions for future work.

8. Conclusion

This work has presented a systematic simulation study of the quantum-confined Stark effect in type-II InAs/GaSb multiple quantum wells across the technologically relevant 5–15 nm thickness range under electric fields up to 200 kV/cm. The principal contributions are: (1) a comprehensive parametric dataset of energy shift, oscillator strength, exciton lifetime, absorption spectra, and wavelength-shift contour map that covers the full mid-IR design space for this material system; (2) derived device figures of merit —modulation depth and extinction ratio—that directly connect simulation output to measurable device performance, with MD values of 5.4–11.2 dB and ER of 4.9–9.8 dB across the studied thickness range; and (3) a Monte Carlo sensitivity analysis demonstrating that ± 15% parameter variation leads to a 2.2-dB spread in modulation depth, setting the required process-control window for reproducible device fabrication.

The results confirm a fundamental design trade-off: thicker wells maximise spectral tunability (Δλ up to ~ 0.7 μm) but reduce zero-field absorption efficiency, while thinner wells offer stronger absorption at the cost of limited tuning range. The modulation-depth crossover point near L = 10 nm, where MD exceeds 8 dB with a Δλ of ~ 0.4 μm, represents an attractive operating regime that balances both requirements for practical electro-absorption modulators. These findings provide a quantitative roadmap for the design of InAs/GaSb-based tunable mid-IR photonic devices, and motivate experimental validation through MBE growth and optical characterisation of the identified optimal well thicknesses.

Declarations

Conflicts of Interest

The authors declare no conflict of interest.

Funding

This research received no external funding.

Author Contribution

Amit Kumar Sinha: Conceptualization, Methodology, Software (Monte Carlo trials), Formal Analysis, Investigation, Visualization, and Writing – original draft.A. M. Khan: Conceptualization, Supervision, Validation, and Writing – review & editing.

Data Availability Statement

The simulation input files, material parameter sets, and extracted data supporting the results of this study are available from the corresponding author upon reasonable request. SILVACO TCAD Atlas

simulation project files are available subject to the applicable software licensing terms.

References

1. Haas, J., Mizaikoff, B.: Advances in mid-infrared spectroscopy for chemical analysis. Annual Rev. Anal. Chem. **9**, 45–68 (2016)
2. Soref, R.: Mid-infrared photonics in silicon and germanium. Nat. Photonics. **4**(8), 495–497 (2010)
3. Chuang, S.L.: Physics of Photonic Devices, 2nd edn. Wiley, Hoboken (2009)
4. Kuo, Y.-H., Lee, Y.-K., Ge, Y., Ren, S., Roth, J.E., Kamins, T.I., Miller, D.A.B.: Harris. Strong quantum-confined Stark effect in germanium quantum-well structures on silicon. Nature. **437**(7063), 1334–1336 (2005)
5. Miller, D.A.B., Chemla, D.S., Damen, T.C., Gossard, A.C., Wiegmann, W., Wood, T.H.: Burrus. Band-edge electroabsorption in quantum well structures: The quantum-confined Stark effect. Phys. Rev. Lett. **53**(22), 2173–2176 (1984)
6. Shen, H., Dutta, M., Fotiadis, L., Newman, P.G., Moerkirk, R.P., Chang, W.H.: Sacks. Photoreflectance study of surface Fermi level in GaAs and GaAlAs. Appl. Phys. Lett. **57**(22), 2118–2120 (1990)
7. Hasbullah, N.F., Ibáñez, J., Hernández, S., Alvarez-Garcia, J., Izquierdo-Roca, V., Pérez-Rodríguez, A., Morante, J.R., Turyanska, L.: Patanè. Type-II InAs/GaSb quantum well infrared photodetectors: A review. J. Electron. Mater. **40**(8), 1795–1803 (2011)
8. Kroemer, H.: The 6.1 Å family (InAs, GaSb, AlSb) and its heterostructures: a selective review. Phys. E. **20**, 3–4 (2004)
9. Razeghi, M.: Overview of antimonide based III–V semiconductor epitaxial layers and their applications at the Center for Quantum Devices. Eur. Phys. J. Appl. Phys. **23**(3), 149–205 (2003)
10. Yang, M.J., Yang, C.H., Bennett, B.R.: Shanabrook. Evidence of a hybridization gap in 'semimetallic' InAs/GaSb systems. Phys. Rev. Lett. **78**(24), 4613–4616 (1997)
11. Smith, D.L., Mailhiot, C.: Theory of semiconductor superlattice electronic structure. Rev. Mod. Phys. **62**(1), 173–234 (1990)
12. Ramanathan, S., Petersen, G., Wijesundara, K., Thota, R., Stinaff, E.A., Kerfoot, M.L., Scheibner, M., Bracker, A.S., Gammon, D.: Quantum-confined Stark effects in coupled InAs/GaAs quantum dots. Appl. Phys. Lett. **102**(21), 213101 (2013)
13. Khan, A.M., Sharma, M., Khan, M.I., Kattayat, S., Bhardwaj, G., Abu-Samak, M., Saeed, S.H.: Alvi. Optical gain characteristics of a novel InAlAs/InGaAs/GaAsSb type-II nano-heterostructure. Optik. **183**, 842–848 (2019)
14. Roch, J.G., Leisgang, N., Froehlicher, G., Makk, P., Watanabe, K., Taniguchi, T., Schönenberger, C.: Warburton. Quantum-confined Stark effect in a MoS_2 monolayer van der Waals heterostructure. Nano Lett. **18**(2), 1070–1074 (2018)
15. Das, S., Dandu, M., Gupta, G., Murali, K., Abraham, N., Kallatt, S., Watanabe, K., Taniguchi, T.: Majumdar. Highly tunable layered exciton in bilayer WS_2: linear quantum-confined Stark effect

versus electrostatic doping. ACS Photonics. **7**(12), 3386–3393 (2020)

16. De, S., Layek, A., Bhattacharya, S., Das, D.K., Kadir, A., Bhattacharya, A., Dhar, S., Chowdhury, A.: Quantum-confined Stark effect in localized luminescent centers within InGaN/GaN quantum-well-based light-emitting diodes. Appl. Phys. Lett. **101**(12), 121919 (2012)
17. Tang, Y., Gu, J., Liu, S., Watanabe, K., Taniguchi, T., Hone, J., Mak, K.F.: Shan. Tuning layer-hybridized moiré excitons by the quantum-confined Stark effect. Nat. Nanotechnol. **16**(1), 52–57 (2021)
18. Vijay, J., Singh, A.K., Rathi, A.: Near-infrared range tuneability in GaAs-based type-II nanoscale heterostructure emitter. J. Nanophotonics. **15**(4), 046009 (2021)
19. Springholz, G., Wiesauer, K.: Nanoscale dislocation patterning in PbTe/PbSe heteroepitaxy and the consequences for lattice-matched growth. Phys. Rev. Lett. **88**(1), 015507 (2002)
20. Meyer, J.R., Hoffman, C.A., Bartoli, F.J., Ram-Mohan, L.R.: Type-II quantum-well lasers for the mid-wavelength infrared. Appl. Phys. Lett. **67**(6), 757–759 (1995)
21. Vurgaftman, I., Meyer, J.R., Ram-Mohan, L.R.: Band parameters for III–V compound semiconductors and their alloys. J. Appl. Phys. **89**(11), 5815–5875 (2001)
22. Bastard, G.: Wave Mechanics Applied to Semiconductor Heterostructures. Les Éditions de Physique, Ulis (1988)
23. Kuo, Y., Li, J., Michalet, X., Chizhik, A., Meir, N., Bar-Elli, O., Chan, E., Oron, D., Enderlein, J., Weiss, S.: Characterizing the quantum-confined Stark effect in semiconductor quantum dots and nanorods for single-molecule electrophysiology. ACS Photonics. **5**(12), 4788–4800 (2018)
24. Walters, G., Wei, M., Voznyy, O., Quintero-Bermudez, R., Kiani, A., Smilgies, D.-M., Munir, R., Amassian, A., Hoogland, S.: Sargent. The quantum-confined Stark effect in layered hybrid perovskites mediated by orientational polarizability of confined dipoles. Nat. Commun. **9**(1), 4214 (2018)
25. Zhang, Z., Fan, Y., Ma, X., Wang, J., Guo, Y., Li, Y., Zhao, M.: Synergizing internal electric field and quantum-confined Stark effect for customized carrier dynamics in two-dimensional heterostructures. J. Catal. **442**, 115877 (2025)
26. Yang, S., Sun, X., Zhou, F., Kang, J., Li, M., Liu, X., Yan, H., et al.: Giant built-in electric field enabled quantum-confined Stark effects. Adv. Photonics. **7**(5), 056003 (2025)
27. Turunen, M., Brotons-Gisbert, M., Dai, Y., Wang, Y., Scerri, E., Bonato, C., Jöns, K.D., Sun, Z.: Gerardot. Quantum photonics with layered 2D materials. Nat. Reviews Phys. **4**(4), 219–236 (2022)
28. Park, K., Deutsch, Z., Li, J.J., Oron, D., Weiss, S.: Single-molecule quantum-confined Stark effect measurements of semiconductor nanoparticles at room temperature. ACS Nano. **6**(11), 10013–10023 (2012)

Figures

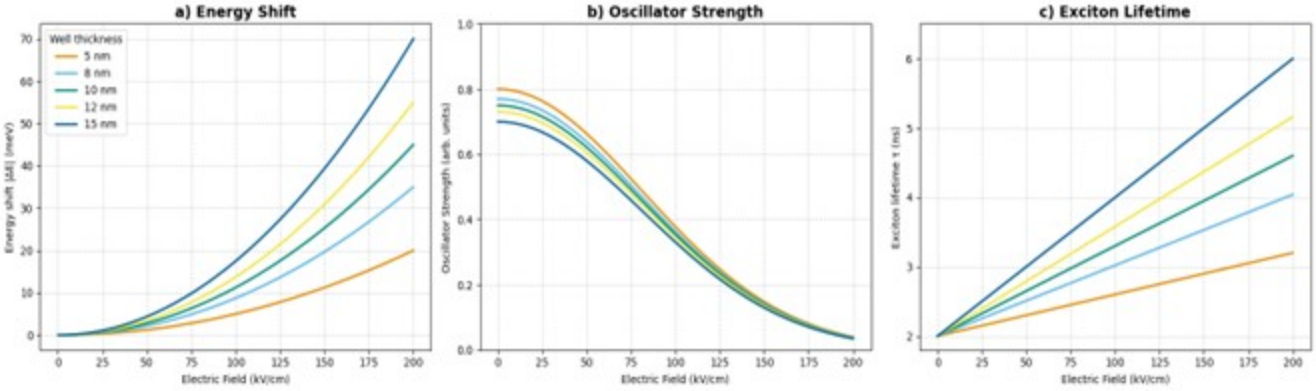


Figure 1

presents the three primary QCSE observables as functions of applied electric field for well thicknesses L = 5, 8, 10, 12, and 15 nm.

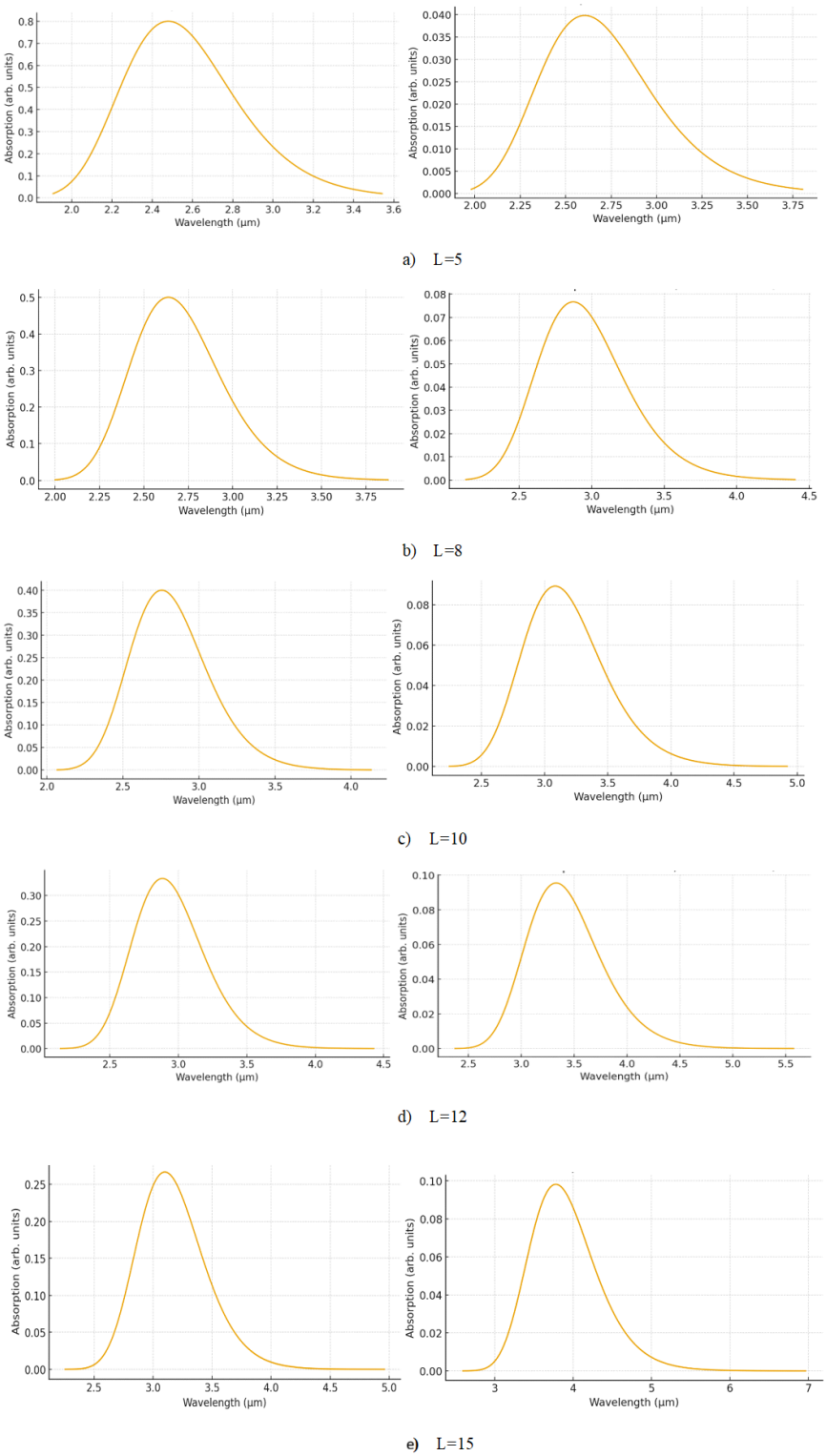


Figure 2

Simulated absorption spectra for each L = 5, 8, 10, 12, 15 nm at Field = 0 kV/cm and Field = 200 kV/cm

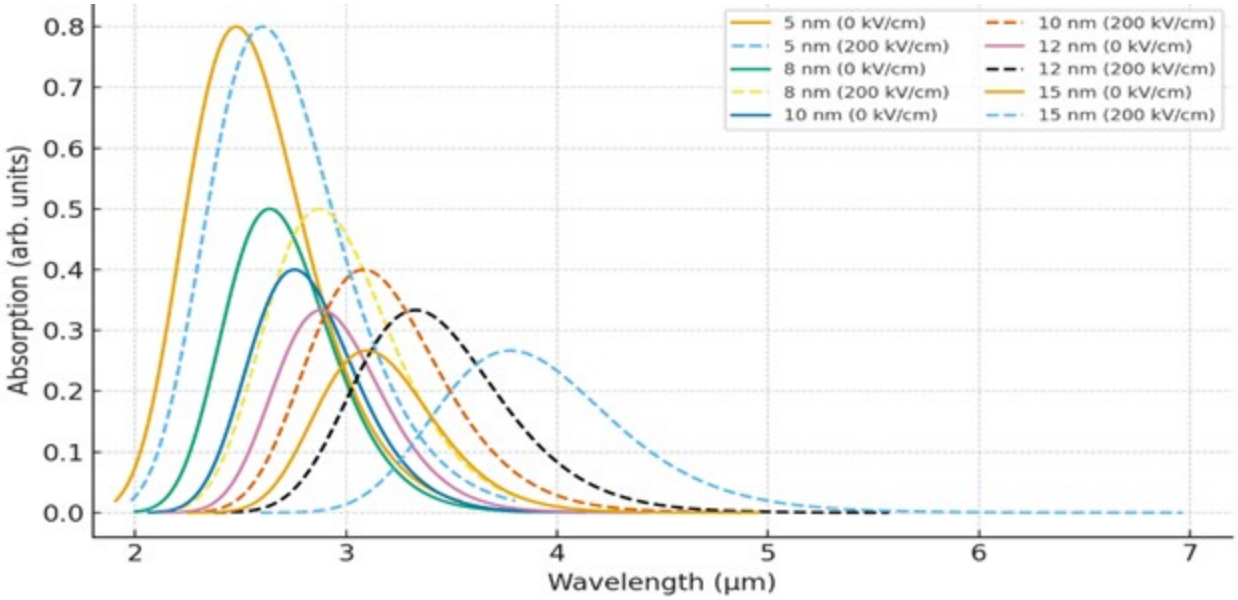


Figure 3

Overall absorption spectra

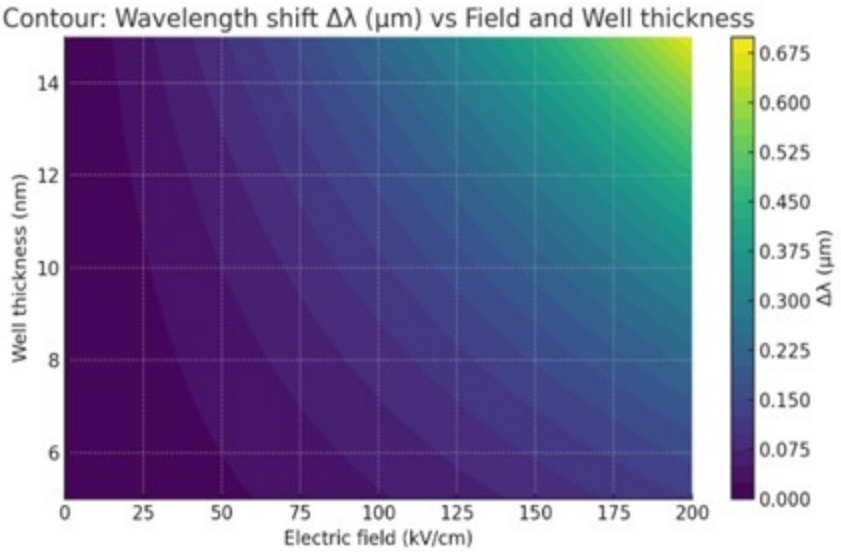


Figure 4

Contour map of wavelength shifts vs electric field and well thickness

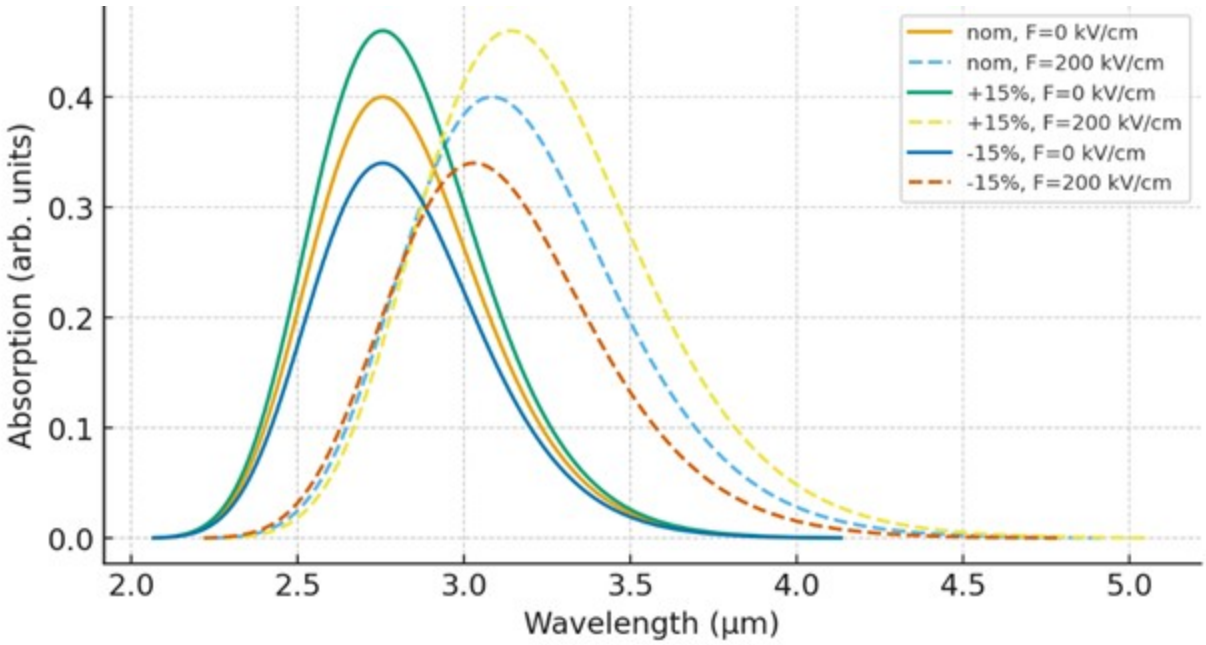


Figure 5

Monte-Carlo sensitivity

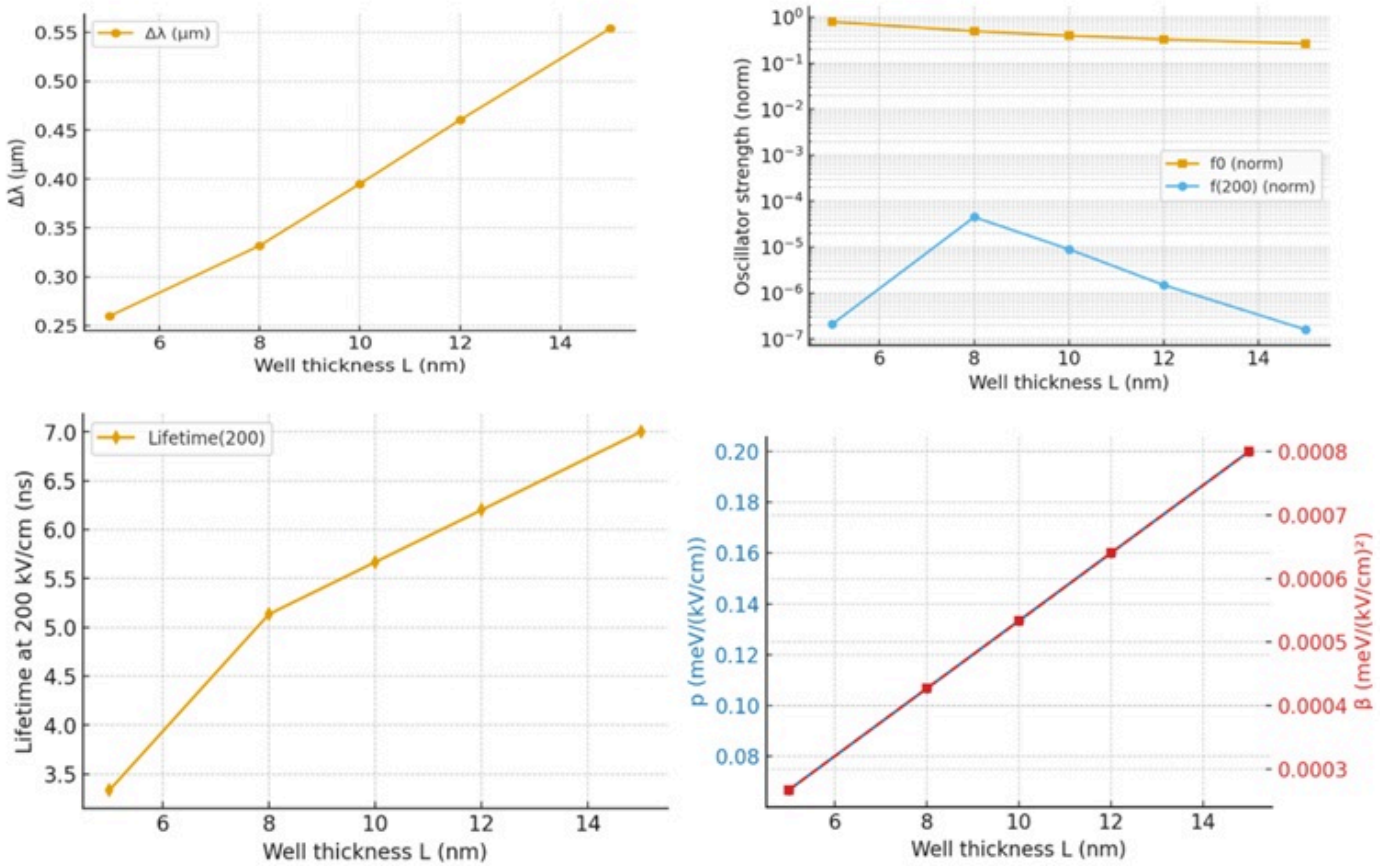


Figure 6

Comparison graph based on parameters